Desalination and Water Treatment
www.deswater.com
doi: 10.1080/19443994.2014.959735

55 (2015) 3424–3445
September

Taylor & Francis
Taylor & Francis Group

CFD prediction of scalar transport in thin channels for reverse electrodialysis

A. Tamburini[a], G. La Barbera[a], A. Cipollina[a], G. Micale[a,*], M. Ciofalo[b]

[a]*Dipartimento di Ingegneria Chimica, Gestionale, Informatica, Meccanica, Università di Palermo, Viale delle Scienze Ed. 6, 90128 Palermo, Italy, email: giorgiod.maria.micale@unipa.it (G. Micale)*
[b]*Dipartimento Energia, Ingegneria dell'Informazione e Modelli Matematici, Università di Palermo, Viale delle Scienze Ed. 6, 90128 Palermo, Italy*

Received 19 April 2014; Accepted 12 June 2014

ABSTRACT

Reverse electrodialysis (RED) is a very promising technology allowing the electrochemical potential difference of a salinity gradient to be directly converted into electric energy. The fluid dynamics optimization of the thin channels used in RED is still an open problem. The present preliminary work focuses on the computational fluid dynamics simulation of the flow and concentration fields in these channels. In particular, three different configurations were investigated: a channel unprovided with a spacer (empty channel) and two channels filled with spacers, one made of overlapped filaments and the other of woven filaments. The transport of two passive scalars, representative of the ions present in the solution, was simulated in order to evaluate concentration polarization phenomena. Computational domain effects were also addressed. Results show that: (i) the adoption of a computational domain limited to a single unit cell along with periodic boundary conditions provides results very close to those obtained in a larger domain; (ii) the woven spacer-filled channel is the best compromise between pressure drop and concentration polarization. Future work will address the inclusion of electrical effects along with the migrative transport of the ions in the channel.

Keywords: CFD; Salinity gradient power; Renewable energy; Reverse electrodialysis; Water; Electric energy; Spacer; Woven; Polarization concentration; Concentration boundary layer

1. Introduction

The interest towards renewable energy is continuously increasing [1]. Power generated from salinity gradients represents a promising renewable energy source and may play an increasing role in the future. The extraction of useful energy from the concentration difference between two saline solutions (Salinity Gradient Power, SGP) has been known for a long time [2] can be performed by means of different technologies such as [3]: pressure-retarded osmosis [4–6], hydrocratic generators [7], vapour pressure difference utilization [8], capacitive mixing based on the double layer expansion technique [9,10], the mixing entropy

*Corresponding author.

Presented at the Conference on Desalination for the Environment: Clean Water and Energy 11–15 May 2014, Limassol, Cyprus

battery [11] and the reverse electrodialysis (RED) [12–17]. According to Logan and Elimelech [18], RED is emerging as a sustainable method for capturing energy from salinity gradients. It is based on the adoption of ionic selective membranes to perform a "controlled" mixing of the two saline solutions thus allowing the "direct" conversion of the electrochemical potential difference into electric energy. Traditionally, river water is employed as the dilute solution and sea water as the concentrated solution. The low ion concentration of the river water causes a large electrical resistance thus limiting the power density obtainable. This represented the main reason of the poor spread of the RED technology in the past. As reported in recent studies [13,19], the employment of sea water as the dilute solution and of brine as the concentrated solution would drastically reduce the electrical resistance of the dilute compartment and enhance the performance of the process. In this regard, each desalination plant may be coupled with a RED process in order to provide both fresh water and electric energy.

The EU-FP7 funded REAPower project [20] is devoted to build a RED pilot plant employing brine and sea water as feed solutions. One of the main aims of the project concerns the choice of the geometrical configuration maximizing the process performance. As in many other separation processes, polarization phenomenon may greatly impair the process' driving force and the relevant power density output. In this regard, fluid mixing promotion within the channel is known to reduce the polarization issues. On the other hand, this is usually made at the cost of increased pressure drops which may affect the process feasibility. Therefore, an optimization of the geometry from the point of view of fluid dynamics is needed: the aim is to find the best compromise between polarization reduction and pumping cost increase, thus leading to an enhancement of the net power density output.

Computational fluid dynamics (CFD) is known to be a powerful tool that can be used to address issues of this kind. It is commonly employed for studying other membrane separation processes such as membrane distillation (MD) [21–23] and reverse osmosis (RO) [24,25].

One of the first attempts to model the mass transport in empty channels separated by selective membranes using CFD was made by Wiley and Fletcher [24]. They carried out two-dimensional simulations to predict the flow field and the concentration polarization for the case of pressure-driven membrane separation processes (as RO and ultrafiltration). Few years later, Santos et al. [26] predicted via CFD the flow and the concentration field for the case of membrane filtration processes. In particular, 12 different spacer structures (ranging from single-layer to two-layer overlapped rectangular filaments spacers) were investigated under different hydrodynamic conditions. Results showed that the number of longitudinal filaments (i.e. parallel to the main fluid direction) does not significantly influence the flow patterns and the flow regime: the transverse filaments are mainly responsible for variations in the flow and concentration fields. Wardeh and Morvan [25] proposed a computational model to investigate different channel-spacer configurations for the case of RO. In particular, two transverse cylindrical filament arrangements were studied: in the first case, the filaments (in a single layer) were placed midway between the channel walls ("submerged" case); in the second configuration, the filaments were alternatively attached to each of the channel membranes ("zigzag" case). The mass transfer efficiency provided by the zigzag configuration was found to be higher than that of the submerged configuration at all the conditions investigated. Also, the results obtained with the submerged configuration were found to be similar to those of a spacer-less channel. Shakaib et al. [27] investigated via CFD the effect of spacer geometry on fluid dynamics and mass transfer in feed channels of spiral wound membrane separation modules. Their results showed that the flow becomes periodic and mass transfer coefficients settle after 3–4 filaments. Spacers with filaments inclined with respect to the channel axis (diamond configuration) generate a zigzag flow path and greatly enhance the mass transfer rates. They concluded that these spacers exhibited the best performance and were the most suitable for spiral wound modules.

On the other hand, only few studies have been devoted to the CFD prediction of the flow in channels to be devoted to RED applications [28–33]. Such channels are so thin, compared to those for RO and MD, that the Reynolds number is much lower, and thus, different flow fields are typically obtained. Only a very few studies have investigated spacers made of woven filaments, despite the fact that many of these are commercially available. All these aspects are addressed by the present work that can be considered as an attempt to simulate both the flow and the concentration (passive scalar) field in spacer-filled channels at the RED scale. This work focuses on how the spacer type can affect the concentration distribution aiming at finding the best compromise between pressure drop and concentration polarization at RED scale.

2. Systems under investigation

A plane channel 400 μm thick and 15.4 cm long and wide (common sizes in small electrodialysis and RED plants) was investigated. In order to study how the arrangement of the spacer filaments affects flow dynamics and the polarization phenomena, different channel configurations were taken into account:

(1) Empty (i.e. spacer-less) channel.
(2) Spacer-filled channels.

(1) The empty channel was investigated as a reference case.
(2) Two different types of symmetrical net spacer-filled channels were investigated:

   (a) a commercial diamond spacer supplied by Fumatech (Fig. 1), made by woven cylindrical filaments;
   (b) a corresponding (i.e. with the same filament diameter and pitch) ideal spacer made by overlapped filaments. This configuration was investigated since overlapped net spacers are largely employed in many membrane separation processes [26,34–36]. Since the fluid dynamics in RED processes is not well established and optimized, it is highly recommended to study also geometrical configurations which are not yet commercially available. From this perspective, CFD may be used as a powerful predictive tool for the RED process design.

For both spacers, the distance between two parallel filaments is 1.1 mm, the filament diameter is 0.2 mm and the angle formed by two crossing filaments is 90˚.

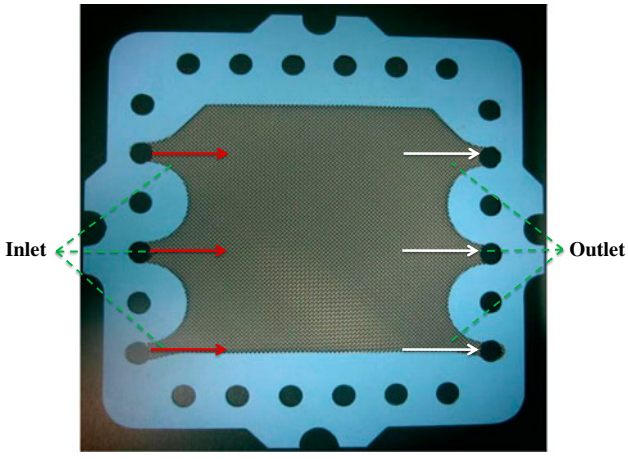

Fig. 1. Woven spacer supplied by Fumatech.

The computational representation of these two net spacers can be observed in Fig. 2. These configurations were already investigated by the present authors in a previous work [29] where additional details can be found.

For every channel configuration, several simulations were performed. Particular attention was paid to the velocity range typically encountered in ED and RED processes (up to about 3 cm s^{-1}), yielding steady laminar flow for all the test cases investigated (see next section). Similarly, concerning pressure drops, computational studies were focused on the typical range of ED/RED processes (up to 0.1 bar m^{-1}). Since different geometries involve different velocities at a constant flow rate, the results will be compared at the same residence times of the fluid within the channel. The tests carried out are reported in Table 1.

The fluid simulated was water at 25˚C with a constant density (997 kg m^{-3}) and viscosity (0.0008899 kg m^{-1} s^{-1}). In order to compare the differences in transport phenomena between the channel configurations, two scalars (A and C), representative of the two ionic species, anionic and cationic, were considered. Inlet concentrations and diffusivity coefficients were chosen as reported in Sections 4.1 and 4.2. Since the Schmidt number ($Sc = \mu/\rho D$) of the two scalars is quite high (about 840 and 550 for, respectively, scalar C and scalar A), it is possible to consider them as "simulated dye tracers" dispersed in water since their transport is directly linked to the flow field inside the channel.

A sketch of the system under investigation (part of a RED stack) is reported in Fig. 3. The aim of the present preliminary work is to compare the performance of different channel configurations for RED in terms of mixing promotion rather than predicting the real behaviour of a real RED channel where charged species and electrical phenomena are present. In this regard, the present approach does not consider the electrical nature of ions, but, on the other hand, makes use of two scalars whose properties (diffusivity and concentration) are similar to those of the ions typically transported in a real RED channel.

3. Modelling

The continuity and momentum equations for the three-dimensional (3D) flow of a Newtonian and incompressible fluid are:

$$\vec{\nabla} \cdot \vec{u} = 0 \tag{1}$$

$$\rho \frac{\partial \vec{u}}{\partial t} + \rho \vec{u} \vec{\nabla} \cdot \vec{u} = -\vec{\nabla} P + \mu \nabla^2 \vec{u} + \vec{F} \tag{2}$$

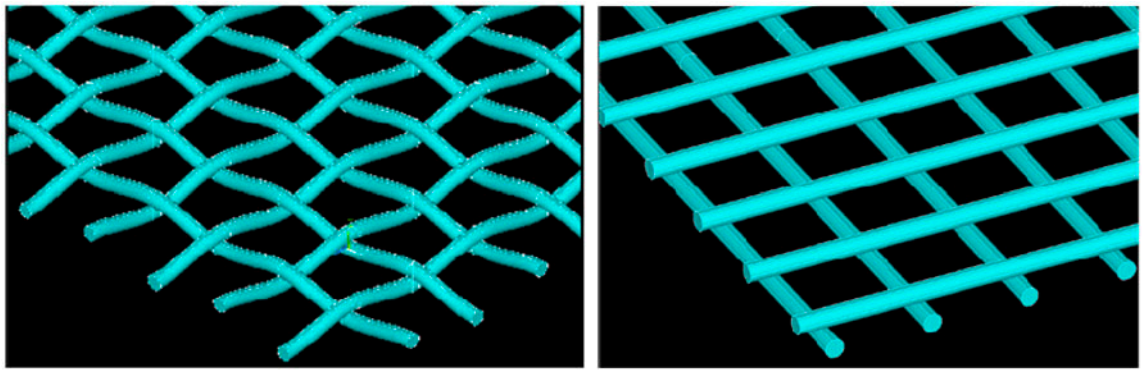

Fig. 2. Computational representation of the (left) woven net spacer and of the (right) overlapped one.

Table 1
Investigated cases: residence times are referred to a channel 15.4 cm long. Velocity values refer to hexahedral (empty channel) and hybrid grids (spacer-filled channel). Reynolds number is calculated in accordance with the definition by Shock and Miguel [37]

	Empty		Overlapped		Woven	
Residence time τ (s)	Average velocity (m s^{-1})	Re (–)	Average velocity (m s^{-1})	Re (–)	Average velocity (m s^{-1})	Re (–)
0.5	0.30855	276.54				
1	0.15428	138.27				
2	0.07714	69.13				
3.5	0.04408	39.50	0.02863	21.76		
7.5	0.02057	18.43	0.01336	10.15	0.01323	9.98
5	0.01029	9.22	0.00668	5.08	0.00662	5.00
30	0.00514	4.60	0.00334	2.54	0.00331	2.50
60	0.00257	23.03	0.00167	1.27	0.00165	1.25
120	0.00129	1.15	0.00084	0.64	0.00083	0.63
180	0.00064	0.57	0.00042	0.32	0.00055	0.42
360	0.00032	0.28			0.00028	0.21

where μ is the viscosity, ρ is the density, P is the pressure and $\vec{F}$ is a force per unit volume. Both transient and steady-state simulations were performed.

Transient simulations were carried out in accordance with the Courant criterion; seven iterations were found to be sufficient to allow the residuals to settle before the next time step. The solutions obtained were stationary, thus confirming the assumption of steady laminar flow. For the case of steady-state simulations, the number of total iterations was chosen in order to guarantee that all the normalized root-mean-square residuals fell below 10^{-6}; typically from 200 to 2,000 iterations were required.

The scalar transport within the computational domain was modelled via the following equation:

$$\frac{\partial C_i}{\partial t} + \vec{\nabla} \cdot (C\vec{u}_i) = D_i \vec{\nabla}^2 C_i \tag{3}$$

The index i refers to one of the two different scalars investigated, A or C. The diffusivity of the scalar was assumed to be constant with the scalar concentration.

4. Numerical details and definitions

All simulations were conducted by the ANSYS-CFX13® code [38]. It is one of the latest development of a long suite of finite volume CFD codes which have successfully been applied through the years by the authors' research group to a variety of fluid dynamics problems [39,40], including mixing in spacer-filled channels [29,32].

In its current version, the code uses a finite volume approach and a co-located (non-staggered) grid layout, such that the control volumes are identical for all transport equations. Since naïve co-located methods lead to a decoupled (checkerboard) pressure

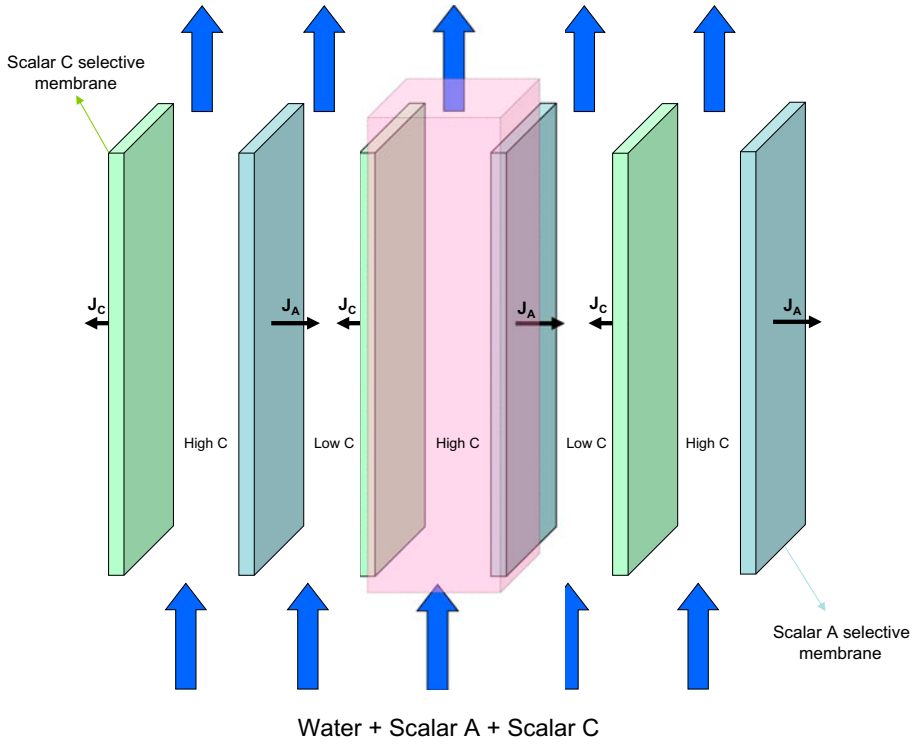

Fig. 3. Portion of a typical RED stack. The coloured region indicates the domain under investigation.

field [41], the Rhie and Chow [42] discretization method for the mass flows is used here to avoid this decoupling. Solution fields and other properties are stored at the mesh nodes (vertices of the control volumes); finite element type shape functions are used to approximate the solution field or the solution gradients at integration points, as required by the evaluation of the various terms of the discretized transport equations.

The code uses a coupled solver, in which the hydrodynamic equations for the three velocity components and pressure are treated as a single large system. A multigrid (MG) accelerated incomplete lower upper factorization technique is adopted for solving the discrete system of linearized equations. The MG process involves carrying out early iterations on a fine mesh and later iterations on progressively coarser virtual ones; the results are then transferred back from the coarsest mesh to the original fine mesh. To prevent the need to explicitly build a series of different mesh spacings, ANSYS CFX uses an Additive Correction Algebraic MG approach [43], in which the discretization of the non-linear equations is performed (only once) for the finest mesh, while the system of discrete equations for each coarser mesh is formed by summing the finer mesh equations.

In the present simulations, the second-order central interpolation scheme was used for the advection terms. In time-dependent simulations, the time derivative of the generic variable Φ was approximated by the second-order backward Euler scheme.

4.1. Model inputs: inlet concentration, diffusion coefficients and mass flux

4.1.1. Inlet concentration

In the present work only the concentrated channel of a RED stack is investigated. The feed solution for the concentrated channel of a RED unit is traditionally seawater. Recently, the EU-FP7 funded REAPower project [20] has proposed the use of the brine as the concentrated solution: this project has led to the construction of a RED pilot plant next to the Trapani desalination plant (Italy). Thus, the brine composition was obtained from that of the plant and is reported in Table 2 along with the molecular weights and the concentrations of the main ionic species. Clearly, the total number of equivalents is equal for positive and negative species in accordance with the electroneutrality principle.

As anticipated in the former section, only two scalars (A and C) were modelled in order to simplify

the CFD simulations. Real salt solutions (as the seawater), presenting a number of ionic species, are commonly studied in the literature as solutions containing NaCl only, both in experimental and in modelling works [44–46]. Thus, scalar A is defined as a somewhat "fictitious" chloride anion representing all the anionic species present in the brine as a whole; similarly, scalar C is a "fictitious" sodium cation representing all the positive ions. Therefore, the inlet concentration of scalar A is calculated by adding up the mass concentrations of all anions, yielding 252.3 g l^{-1}; similarly, the scalar C inlet concentration is equal to the sum of the mass concentration of cations, yielding 115.5 g l^{-1}.

4.1.2. Diffusion coefficients

On the basis of the diffusivity of each salt composing the brine in the brine itself [47], a mixed diffusion coefficient can be calculated as in the following:

$$D_{NaCl} = 1.60 \times 10^{-9}\ m^2\ s^{-1}$$
$$D_{MgSO_4} = 0.30 \times 10^{-9}\ m^2\ s^{-1}$$
$$D_{KCl} = 1.80 \times 10^{-9}\ m^2\ s^{-1}$$
$$D_{MgCl_2} = 1.26 \times 10^{-9}\ m^2\ s^{-1}$$

$$D_{mixed} = \frac{\sum_{i=1}^{4} C_i \cdot D_i}{C_{tot}} = 1.345 \times 10^{-9} m^2\ s^{-1} \quad (4)$$

The diffusion coefficient of the scalars A and C in the brine is estimated by referring to this D_{mixed} term and to the infinite dilution diffusion coefficients of sodium and chloride ions in a water solution [47]:

$$D^{\circ}_{Na^+} = D^{\circ}_{C} = 1.33 \times 10^{-9}\ m^2\ s^{-1}$$
$$D^{\circ}_{Cl^-} = D^{\circ}_{A} = 2.03 \times 10^{-9}\ m^2\ s^{-1}$$

In particular, D°_A and D°_C result from the following system:

$$\begin{cases} \frac{C_A \cdot D_A + C_C \cdot D_C}{C_A + C_C} = D_{mixed} \\ \frac{D_A}{D_C} = \frac{D^{\circ}_A}{D^{\circ}_C} \end{cases} \quad (5)$$

$$D_A = 1.56 \times 10^{-9}\ m^2\ s^{-1}$$
$$D_C = 1.02 \times 10^{-9}\ m^2\ s^{-1}$$

In order to quantify the error caused by the approximated calculation of D_A and D_C, several simulations were performed by letting the diffusion coefficients vary. It was found that changes of ± 25% in diffusivities cause differences less than 4% in polarization factors.

4.1.3. Mass flux through the membranes

A complete simulation of ion transport would require a modelling not only of the convective and diffusive processes in the fluid, but also of the phenomena occurring within the membrane and at its boundaries. Since, in the present study, the attention is focused on the transport phenomena occurring in the fluid, simplified boundary conditions were directly imposed at the walls (fluid–membrane interfaces). In this regard, two possible standard conditions could be chosen: uniform wall concentration or uniform wall mass flux. Both boundary conditions are only idealizations of the real situation expected in the channel, where both the wall concentration and the wall mass flux will exhibit a spatial variations related (i) to the shape of the spacer, if present and (ii) to the large-scale concentration gradient along the flow direction. However, among the two, the condition of uniform mass flux was judged to be more realistic taking account of the low fluid resistance and to the short length of the channels.

In this regard, Veerman et al. [44] found an almost linear variation of the concentration along the length (i.e. main flow direction) of a typical RED channel thus resulting in an almost constant mass flux orthogonal to the membrane. Of course, the two phenomena are equivalent as easily explained by a simple mass balance on a parallelepiped channel (Fig. 4). When steady-state conditions are achieved, the differential mass balance of scalar A (identical considerations can be done for scalar C) is:

Table 2
Data of brine deriving from the Trapani desalination plant

	K^+	Mg^{++}	Na^+	Cl^-	SO_4^-
Molecular weight (g mol^{-1})	39.1	24.3	23.0	35.5	96.0
Concentration (g l^{-1})	10.0	47.0	58.5	192.3	60.0
Concentration (mol l^{-1})	0.256	1.934	2.544	5.418	0.625
Equivalent concentration (eq l^{-1})	0.256	3.868	2.544	5.418	1.250

$$\frac{dC_A}{dz} = -\frac{w}{Q} J_A \tag{6}$$

where Q is the flow rate ($m^3\ s^{-1}$), J_A is the material flux through the membrane selective to scalar A, w is the channel width and z is the main flow direction. Notably, the flux is outgoing from the computational domain since a concentrated channel is taken into account.

Actually, the slope of the curve C_A – z in Veerman et al. work [44] decreases only slightly along the z direction: this means that the flux J_A decreases slightly along the channel since the driving force decreases, but this effect can reasonably be neglected because of the shortness of RED channels in terms of number of transfer units.

Concerning the specific flux value to be employed, Veerman et al. [44] obtained their values of current density and electrolyte mass flux by using a RED stack supplied with seawater and river water. The adoption of seawater and brine, with their lower electrical resistance, along with the expected membrane performance improvement and stack optimization, figured out by the REAPower project objectives, suggested us to adopt a mass flux of one order of magnitude higher than that reported by Veerman et al. [44]. Thus, a molar flux of 3.93×10^{-3} mol $m^{-2}\ s^{-1}$ was used for both the scalars, which corresponds to mass fluxes

$$J_C = 9.03 \times 10^{-5}\ \text{kg}\ m^{-2}\ s^{-1}$$
$$J_A = 1.39 \times 10^{-4}\ \text{kg}\ m^{-2}\ s^{-1}$$

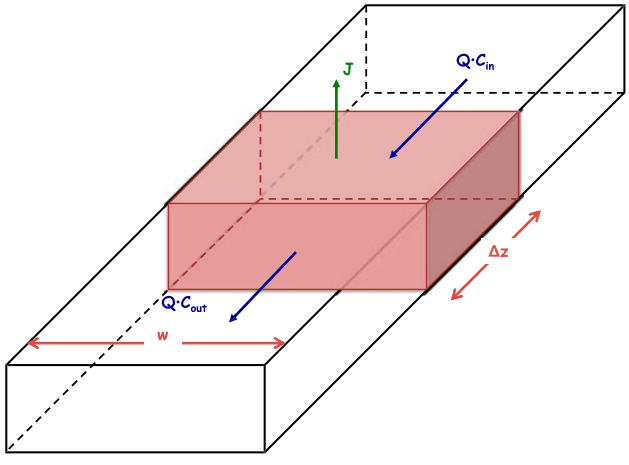

Fig. 4. Parallelepiped segment of a typical RED channel.

4.2. Unit cell and strip (multi-cell) approach

The flow field in a spacer-filled channel is characterized by very small structures requiring a very high discretization degree to be properly predicted. As a consequence, the simulation of an entire experimental channel 15.4 cm long and wide would require an excessive number of computational cells and prohibitive simulation times. In order to sort this issue out, it is very common in the literature to adopt the *Unit Cell approach* [26,31,32,48,49]. Apart from the regions next to the inlet, the outlet or the lateral boundaries of the channel, the flow field is periodic so that only a very small domain (*Unit Cell*, containing one or more spacer meshes) is simulated as representative of the whole channel. This type of modelling is broadly used in CFD studies [48,50] and is widely accepted by the scientific community. As shown in Fig. 5, different Unit Cells can be employed for the same spacer net. The cell chosen here was type I, the same adopted by Li and Tung [49].

The features of the Unit Cells investigated are shown in Fig. 6 for the cases of a woven spacer (a) and an overlapped spacer (b). An identical unit cell was employed also for the case of the empty channel (c) for comparison purposes.

Translationally, periodic boundary conditions were imposed on the surface couples perpendicular to the main fluid flow direction (Z-axis) and to the X-axis. No-slip boundary conditions were imposed on the filaments' surfaces and on the surfaces perpendicular to the Y-axis (membrane surfaces), which were defined as walls. A pressure gradient directed along the main flow direction was imposed as the source term $\vec{F}$ in the momentum equations. Different simulations at different values of the pressure gradient were carried out. Corresponding values of fluid velocities were obtained by the simulation results. Full details can be found in Tamburini et al. [29].

As an alternative, a strip as wide as one unit cell was built for every channel configuration, as schematized in Fig. 7 (*Multi-Cell Approach*). Fig. 7(a) shows the strip is composed of a number of unit cells glued together and arranged along the main flow direction. Uniform velocity and concentration profiles were imposed at the inlet (upstream face of the first cell): a concentration of 252.3 g l^{-1} for scalar A and a concentration of 115.5 g l^{-1} for scalar C. On the contrary, at the outlet face (downstream face of the last cell) a pressure of 1 bar and zero normal derivative of concentrations were imposed. As in the case of the *Unit Cell*, periodic boundary conditions were imposed on the surfaces perpendicular to the lateral x-direction.

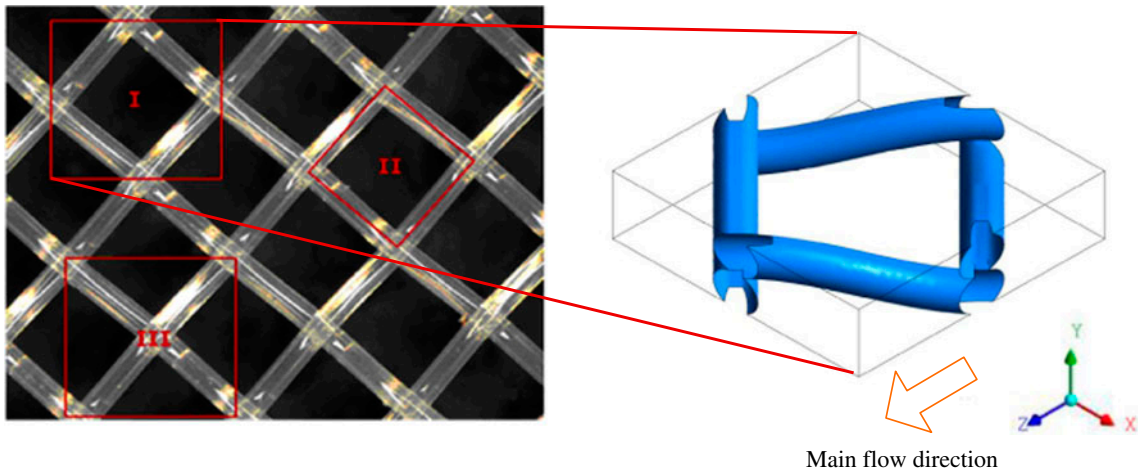

Fig. 5. Different types of unit cell for the woven spacer.

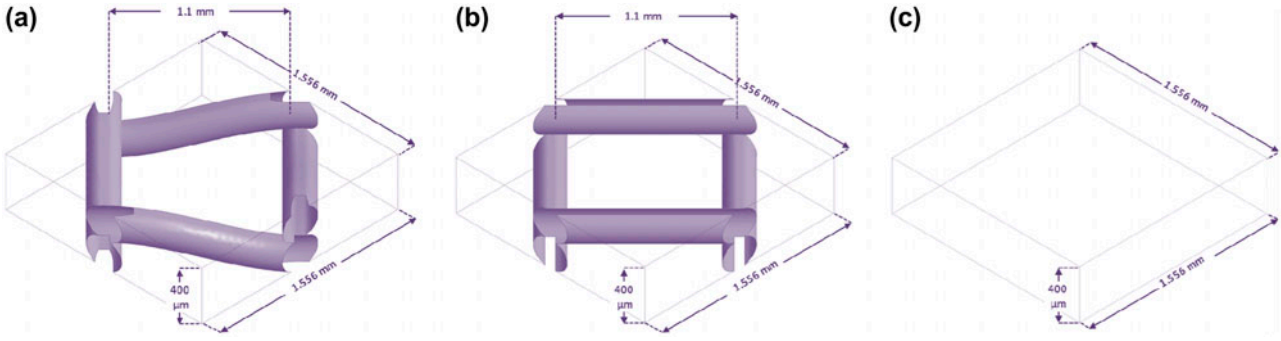

Fig. 6. Unit cell for the (a) woven spacer-filled channel, (b) the overlapped spacer-filled channel and (c) the empty-filled channel.

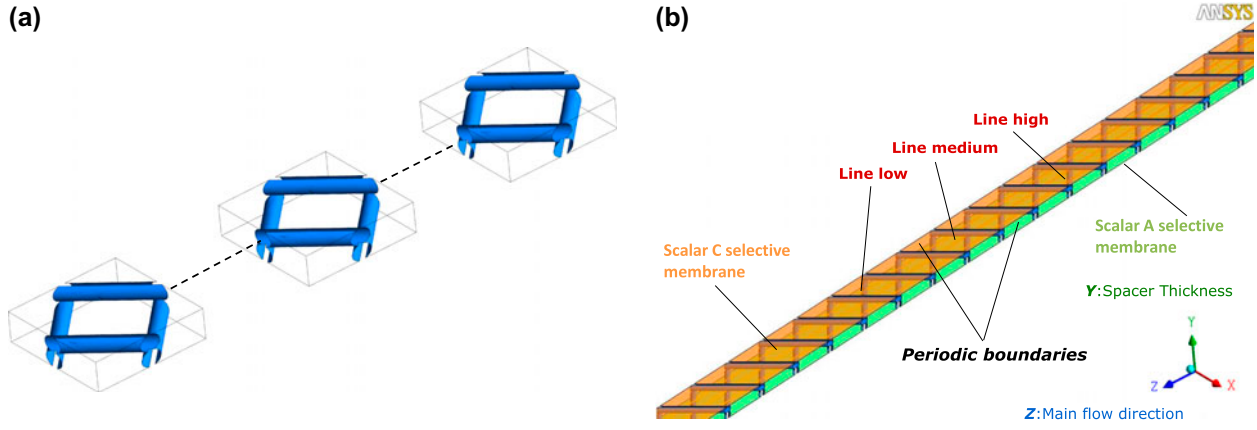

Fig. 7. Strip approach for the overlapped spacer-filled channel. (a) Sequence of unit cells and (b) strip assembled.

Simulation results (in the form of velocity profiles along the line low, medium and high of Fig. 7, not reported for brevity) showed that the flow field was completely developed after only two unit cells, as already found by Shakaib et al. [27]. Therefore, all simulations were conservatively performed by simulating a strip made of nine unit cells.

Since in spacer-filled channels the flow field is quite complex due to the spacer wires, the concentration field is expected to be complex as well. Therefore, nine monitoring lines perpendicular to the surfaces (y direction) and placed in the fifth unit cell (midway between inlet and outlet) were considered in order to study how the concentration polarization varies depending on the position in the unit cell. Their location is shown in Fig. 8.

In the simulations reported in the present work, a computational grid of ~250,000 volumes per unit cell was adopted (so that the computational domain used in the "Multi-Cell" approach was composed of ~2,250,000 volumes). The grid was mainly made up of hexahedral volumes, only in the proximity of the wires the use of some tetrahedral volumes was necessary due to the geometrical complexity of these regions. A previous study [29] showed that the above number of volumes was sufficient to yield practically grid-independent results and that a mostly hexahedral grid was superior to a purely tetrahedral one. The latter findings was reported also by other authors for the case of applications different than RED [51–53].

Notably, a grid of 250,000 computational cells (all composed of hexahedra) was employed also for the empty channel only for coherency purposes; in fact, a grid with ~60,000 nodes was found to provide identical results.

4.3. Quantities characterizing the mixing performance of a spacer

4.3.1. Concentration polarization coefficients θ and θ_w

Polarization coefficients are commonly defined as the ratio of the difference between the concentration values on the two sides of the membrane surface divided by the difference between the bulk concentration values. In the present work, only the concentrated channel is simulated so that an alternative definition of the polarization coefficient was adopted. More precisely, two different polarization coefficients were defined for each monitoring line.

The former (*local concentration polarization coefficient*) is defined as:

$$\theta(x,y,z) = \frac{C(x,y,z)}{C_{max}(x,z)} \tag{3}$$

where C is the local concentration, and C_{max} is the maximum value of local concentration along the monitoring line under consideration.

The latter polarization coefficient (*wall concentration polarization coefficient*) is defined as:

$$\theta_w(x,z) = \frac{C_w(x,z)}{C_{max}(x,z)} \tag{4}$$

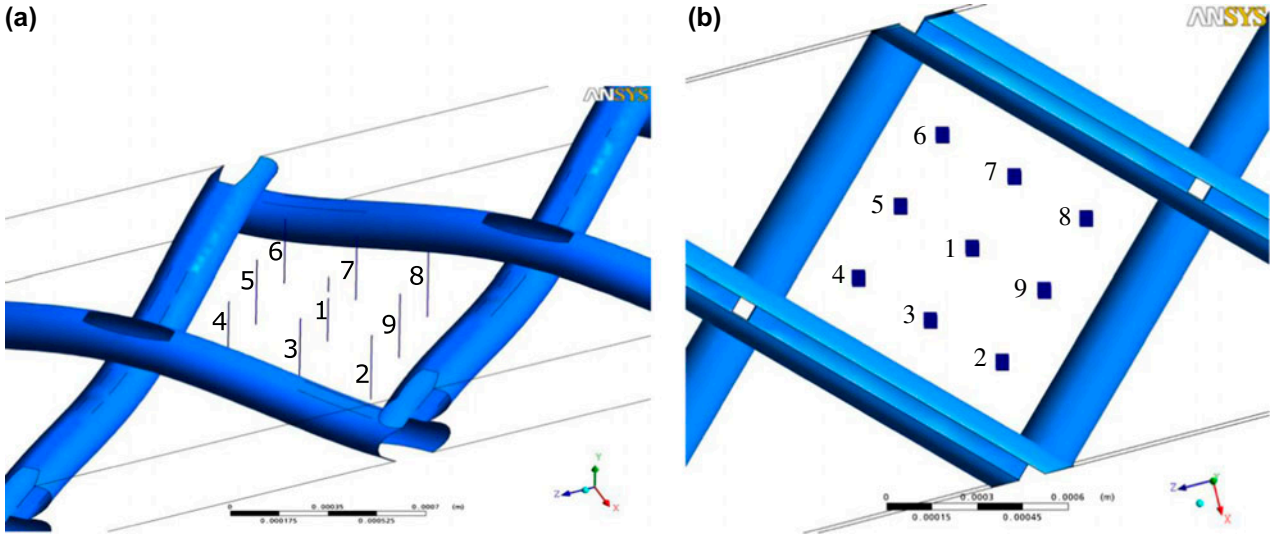

Fig. 8. Monitoring lines for the concentration boundary layer. (a) Woven spacer-filled channel—axonometric view and (b) Overlapped spacer-filled channel—planar view from above.

where C_w is the value of concentration on the membrane surface (the *scalar C selective membrane* for the case of scalar C and the *scalar* A *selective membrane* for the case of scalar A). This wall polarization coefficient varies only along the x and z directions.

4.3.2. Concentration boundary layer thickness δ

An interesting aspect of polarization phenomenon which can be predicted via CFD is the thickness of the *concentration boundary layer*, i.e. the region over which the concentration gradient extends.

In order to quantify such thickness, a commonly adopted definition [54] depicted in Fig. 9 was used. Y/L is the normalized distance from the surface normalized by the channel thickness. It is possible to draw the tangent to the concentration curve at the membrane surface and identify δ as shown in figure.

5. Results and discussion

5.1. Pressure drop for different spacers

In the present work, the unit cell approach is employed for the estimation of the relation between pressure drops and flow rate while the multi-cell approach was employed to evaluate the mass transfer phenomena. Though the unit cell approach is widely used in CFD modelling [49], its results were compared with the corresponding ones obtained by the multi-cell approach for validation purposes. Several simulations were performed using both approaches for each channel configuration. Results are reported in Fig. 10 where a very good agreement between the two approaches can be observed. This comparison confirms that the prediction of the flow field through unit cells instead of larger domain portions (e.g. long strips) allows a large reduction of the computational effort without affecting the reliability of the results.

The predicted pressure drops as functions of the liquid flow rate are summarized in Fig. 11 where it can be observed that: (i) the empty channel provides the lowest pressure drop as expected; (ii) the presence of a spacer clearly enhances the pressure drop; (iii) the woven spacer provides pressure losses higher than the overlapped one; and (iv) all the trends are linear thus confirming the existence of a self-similar flow regime in all the channel configurations at the RED operating range. Notably, the upper limit of $\Delta P/l$ = 0.1 bar m^{-1} investigated was chosen according to the expected operating range of typical RED applications.

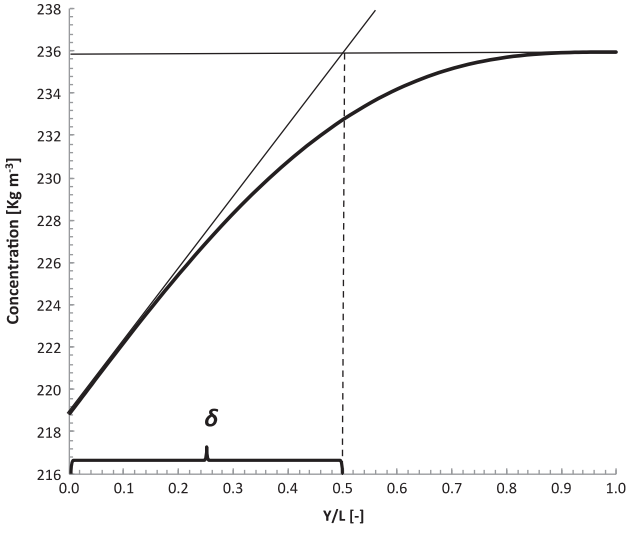

Fig. 9. Typical modelling of concentration boundary layer.

5.2. Polarization concentration phenomena

In this section, all results are obtained using the multi-cell approach. The scalar transport within the channel along with the relevant polarization concentration phenomenon is quantified by assessing the

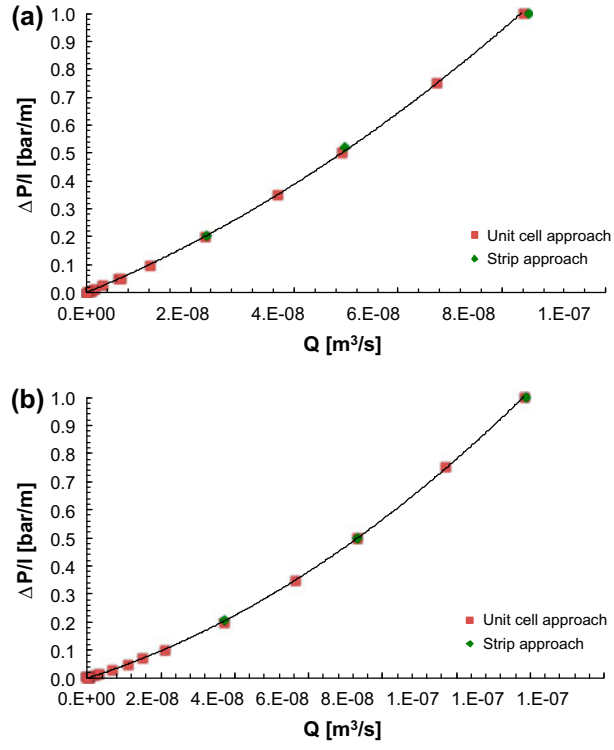

Fig. 10. Validation of unit cell approach: (a) woven spacer and (b) overlapped spacer-filled channel.

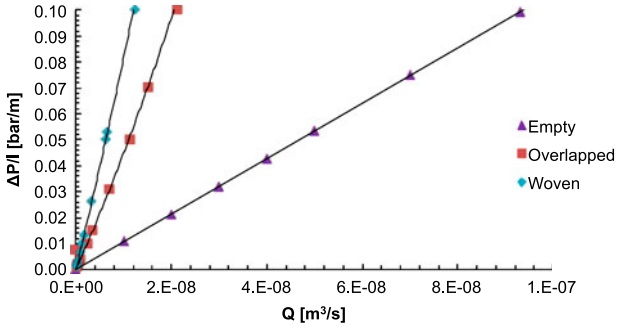

Fig. 11. Pressure drops as a function of the fluid flow rate: comparison among the different channel configurations.

concentration profiles along the nine monitoring lines mentioned in Section 4.2. The corresponding local and wall polarization factors (θ and θ_w) and the concentration boundary layer thickness (δ) are also provided.

5.2.1. Empty channel

As previously anticipated, the empty channel configuration was investigated for comparative purposes.

In Fig. 12, the concentration profiles of scalar A and scalar C along the nine monitoring lines are reported. Of course, since the problem is one dimensional, the concentration profiles are identical for all monitoring lines. Note that, despite the simple geometry of an empty channel, no simple analytical solution for the two species concentrations is available because of the entry effects, which are particularly significant in laminar flow and which are fully taken into account by the present numerical solution.

Also the values of θ_w and δ are independent of the location in the channel and are equal to θ_w = 0.936 (scalar A) or 0.878 (scalar C) and δ/L = 0.458 (scalar A) or 0.414 (scalar C) for a residence time of 60 s.

In order to evaluate how the fluid flow rate affects the concentration polarization, the θ trends along the central monitoring line 1 at a number of different residence times were predicted and the relevant results are reported in Fig. 13.

Clearly, the concentration coefficient profiles are not symmetrical because concentrations were estimated on mass basis (kg m^{-3}) rather than on molar basis.

The higher the liquid flow rate (i.e. the lower the residence time) the lower the concentration polarization. In accordance with Vermaas et al. [55], the process driving force variation with the flow rate may be due to two different contributions: (i) variation of fluid velocities perpendicularly to the membranes; and (ii)

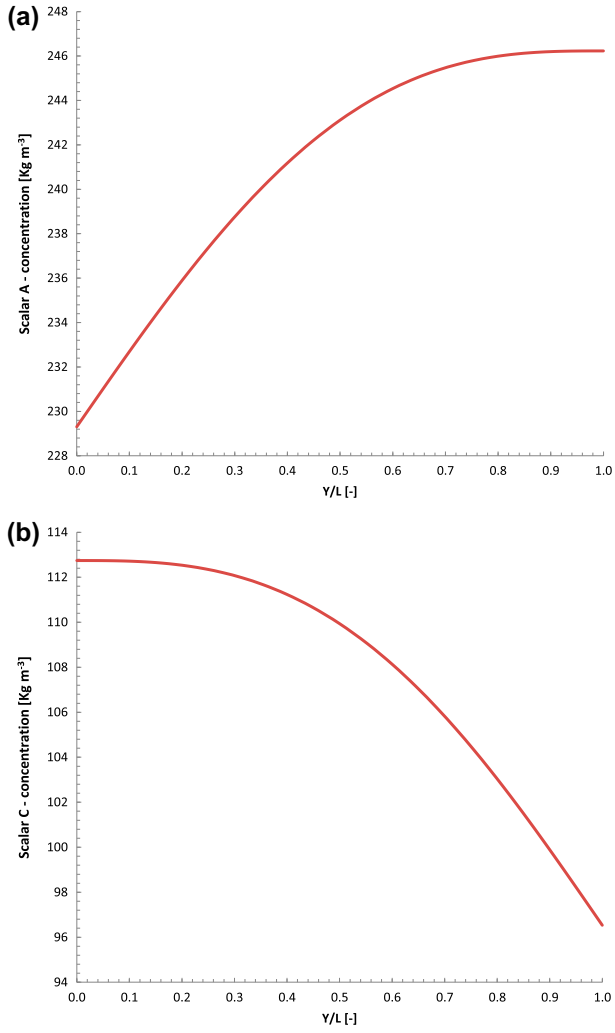

Fig. 12. Concentration profile of (a) scalar A and (b) scalar C along a monitoring line for the case of a residence time equal to 60 s. Empty channel.

variation of the bulk concentration along the main flow direction. Since the fluxes of scalar A and scalar C through the membranes are assumed to be independent of the liquid flow rate (see Section 4.1.3 and the slope of the curves at the membrane boundaries in Fig. 13), the increase of the concentration polarization as the flow rate decreases is linked to a reduction of the bulk concentration only. In fact, in the empty channel only the diffusive transport takes place in the direction perpendicular to the membrane surface as no velocity components are present along this direction.

More specific pieces of information on the polarization are reported in Fig. 14 where the θ_w and the normalized δ vs. residence time are shown. As it can be also inferred from Figs. 13 and 14(a) shows that θ

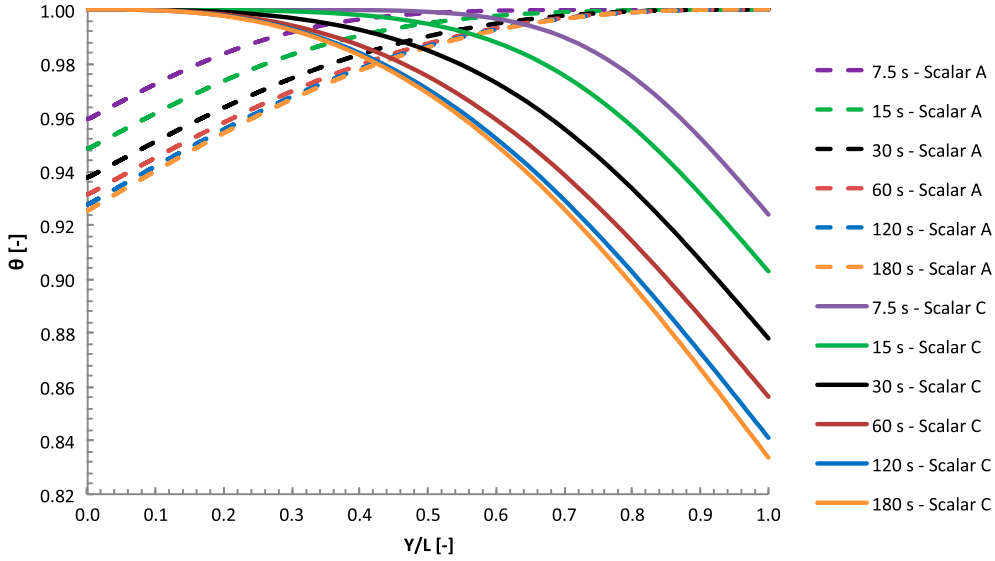

Fig. 13. θ trends along the monitoring line 1 for different residence times. Empty channel.

decreases as the residence time increases as expected: the polarization concentration phenomena are more pronounced when the bulk concentration decreases thus suggesting the adoption of high concentrated solutions as feeds for the process (brine and seawater as concentrated and diluted solutions, respectively) as well as low residence times (i.e. high flow rates or short channels).

Fig. 14(b) shows that an increase of the residence time leads to an increase of δ. Such variation is not surprising since it is in accordance with the assumption of constant outgoing flux: the variation of the difference between the bulk and the wall concentration must be followed by a corresponding variation of the boundary layer thickness. Moreover, δ approaches an asymptotic value of $L/2$ as the residence time increases: this occurrence is confirmed by the exact analytical solution for fully developed flow and concentration profiles.

5.2.2. Woven spacer-filled channel

The employment of a spacer within the channel significantly affects both the flow and the concentration field.

As a difference from the empty channel, the presence of a woven spacer generates a complex flow field composed of velocity components directed in the three spatial directions [29]. Because of this 3D complex flow field, the scalar concentration along some of the monitoring lines orthogonal to the membranes does not exhibit its maximum at the non-permeable membrane (as in empty channels), but at an intermediate zone (Fig. 15). Notably, such result is not in disagreement with the assumption of a zero flux across the non-permeable membrane which only requires a zero derivative of the concentration profiles at this boundary.

A close inspection of Fig. 15 shows some geometrical symmetry between the concentration profiles of the two scalars: the concentration profile of scalar A along a line is similar to that of the scalar C along the line that is geometrically symmetrical to the first one with respect to the Y–Z mid-plane, see Fig. 8. For example, the concentration profile of the scalar A along line 2 is similar to that of the scalar C along line 6, which is geometrically symmetrical to line 2.

Fig. 16 shows the values of θ_w and δ along each monitoring line. As it can be already inferred from Fig. 15, the presence of the woven spacer causes a large heterogeneity of the concentration polarization on the membranes: both θ_w and δ exhibit a significant variation with the spatial position in a unit cell (Fig. 16).

The highest values of δ are located near the zones not shielded by the filaments. For example, for the case of the scalar A, δ values at lines 2, 3 and 9 are larger than the others. The filament is located at the channel top, upstream these lines and scalar A approaches its selective membrane without encountering any obstacles. This results in higher values of δ. Similarly, according to the symmetry previously described, scalar C exhibits the highest δ at lines 5, 6 and 7.

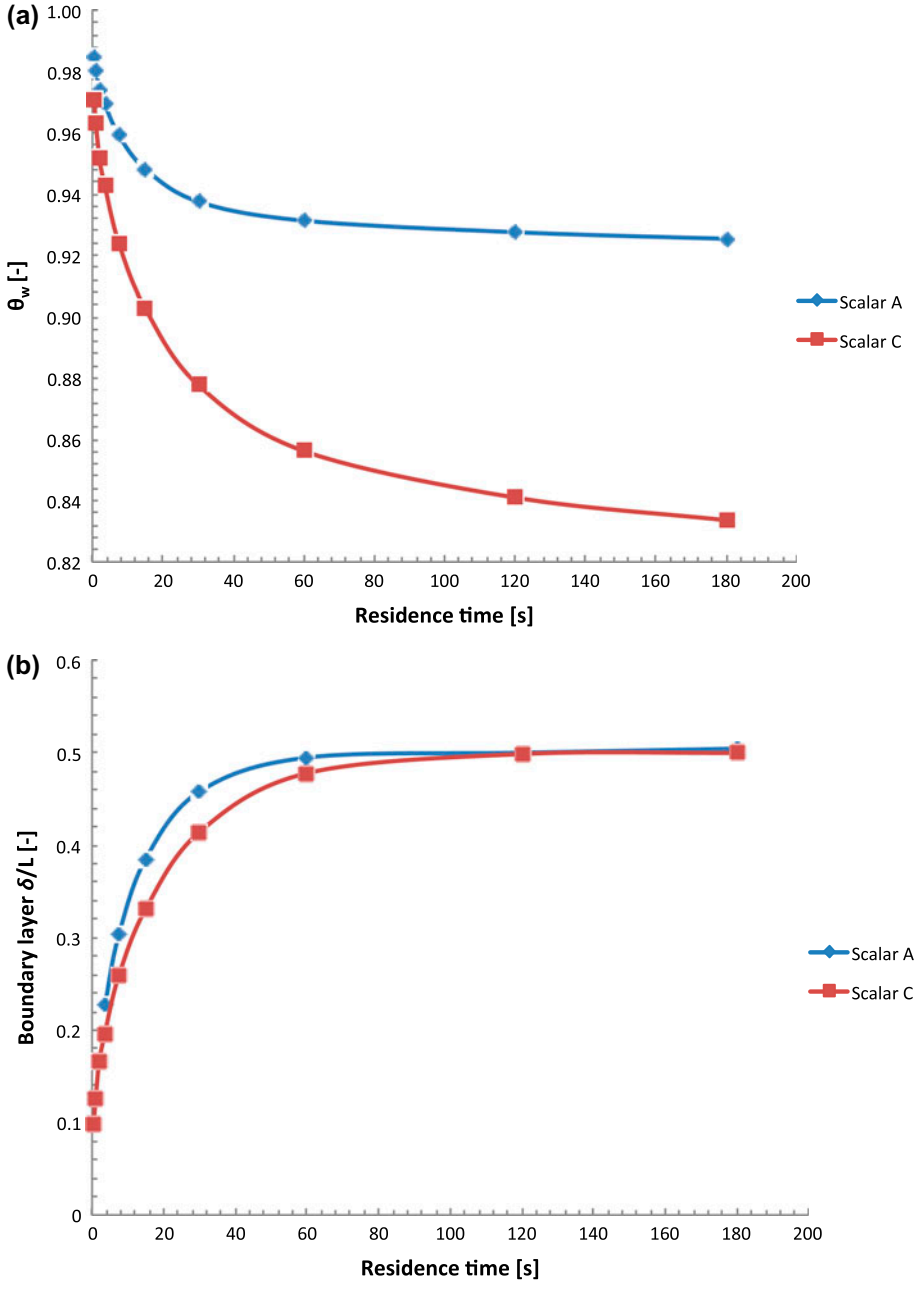

Fig. 14. θ_w (a) and δ (b) vs. residence time along the monitoring line 1. Empty channel.

Fig. 17 reports the θ profiles as a function of the residence time. As it can be seen, the presence of the woven spacer leads to a large reduction of the concentration polarization with respect to the empty channel. All the profiles also show the presence of an inflection point and of a maximum. Interestingly, each maximum is located at a distance from the non-permeable membrane equal approximately to 37% of the channel thickness (140 μm against 400 μm) for any residence time and for both scalars.

In this case, the polarization increase with increasing residence times (decreasing velocity) is due not only to the change in bulk concentration but also to the presence of velocity components directed perpendicularly to the membranes: thus, the two different contributions to the reduction of the process driving force, identified by Vermaas et al. [55], can be found in this case.

Concerning the dependence of δ on the residence time (not reported for brevity), δ values are lower than

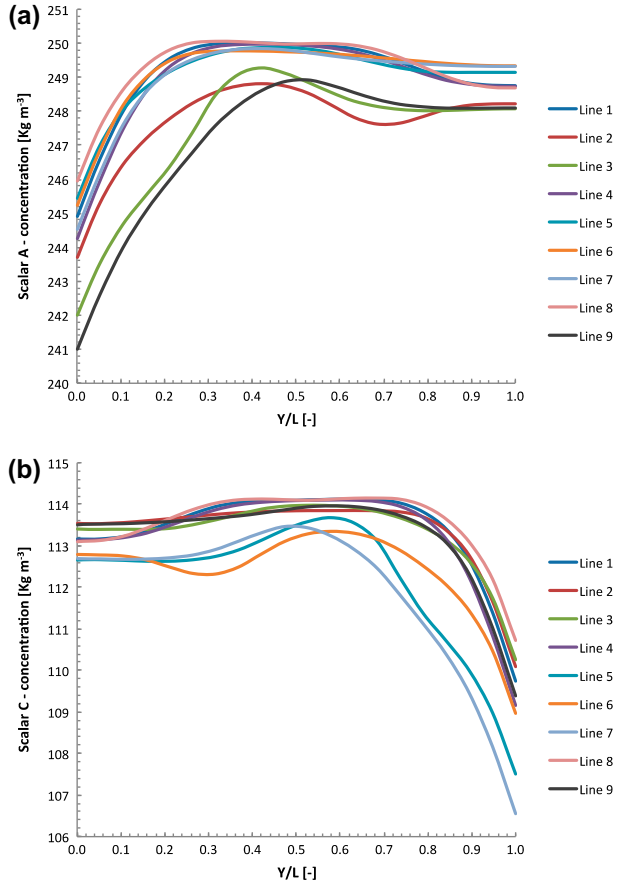

Fig. 15. Concentration profile of (a) scalar A and (b) scalar C along the nine lines for the case of a residence time = 60 s. Woven spacer-filled channel.

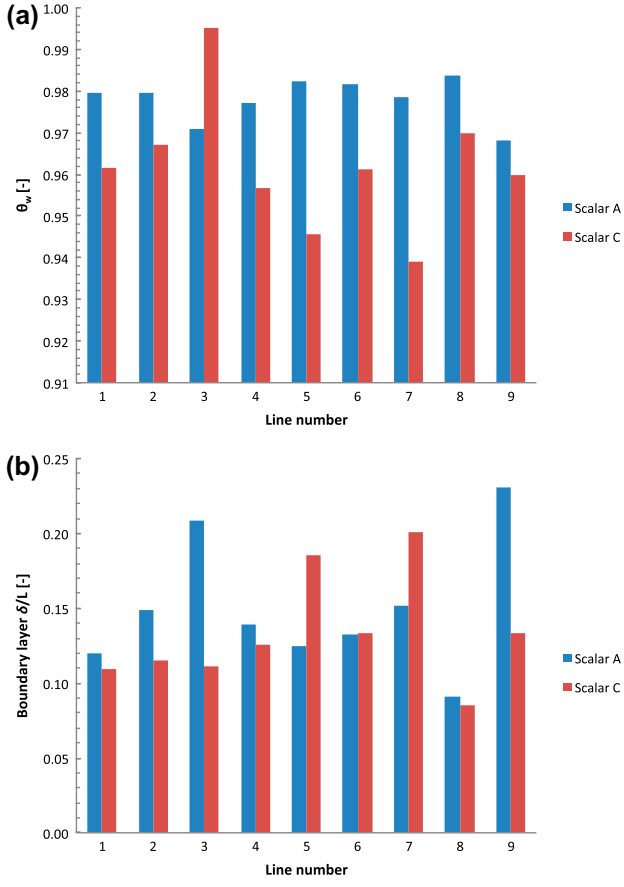

Fig. 16. θ_w (a) and δ (b) values along the nine monitoring lines for the case of a residence time = 60 s. Woven spacer-filled channel.

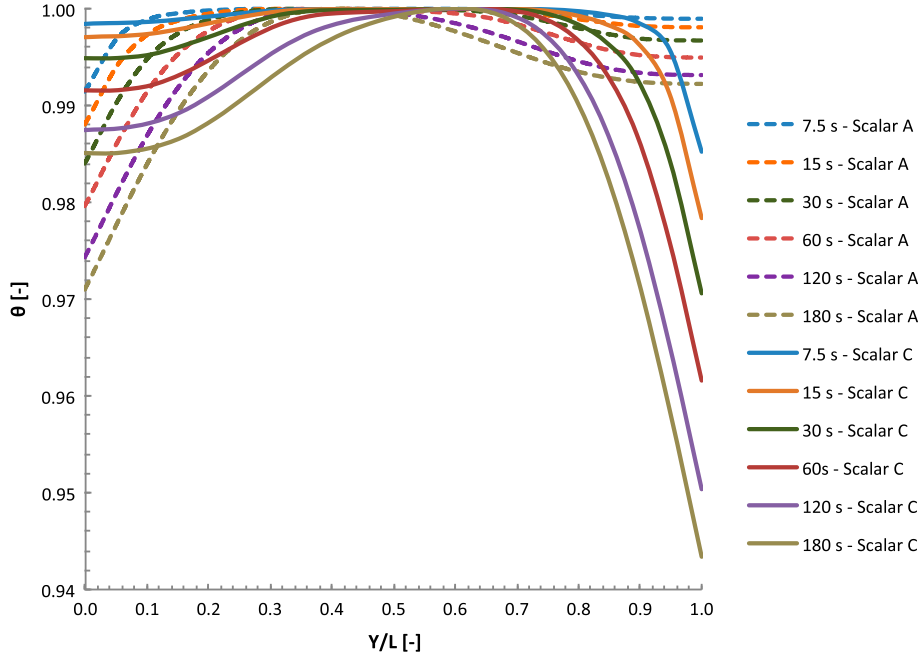

Fig. 17. θ trends along the monitoring line 1 for different residence times. Woven spacer-filled channel.

those of the empty channel. Moreover, δ does not appear to approach a constant value at high residence times.

5.2.3. Overlapped spacer-filled channel

The main difference from the woven spacer concerns the geometrical arrangement of the filament. Such difference leads to significantly different flow fields [29] thus resulting in different pressure drops.

As a difference from the woven spacers, the concentration profiles along the nine monitoring lines orthogonal to the membranes Fig. 18 are quite similar. Such profiles appear to be more similar to those observed in the empty channel than those relevant to the woven spacer-filled channel. For instance, the maximum concentration of each scalar is reached on its non-permeable membrane, as in the empty channel, and not at an intermediate point as in the woven spacer configuration.

In contrast with the case of the woven spacer-filled channel, the flow pattern in the overlapped spacer-filled channel tends to homogenize the concentration profiles along the nine monitoring lines: the histograms of θ_w and δ reported in Fig. 19 show a much more homogeneous distribution compared to the case of the woven spacer-filled channel.

In Fig. 20, the θ profiles along the monitoring line 1 against the fluid residence times are shown. As already stated for the case of the woven spacer, also in this case the reduction of the polarization as the residence time decreases is due to the bulk concentration reduction and to the increase of the velocity components perpendicular to the membrane. Interestingly, the profiles relevant to high residence times exhibit two inflection points. These disappear at the lower residence times. Also, this behaviour is probably due

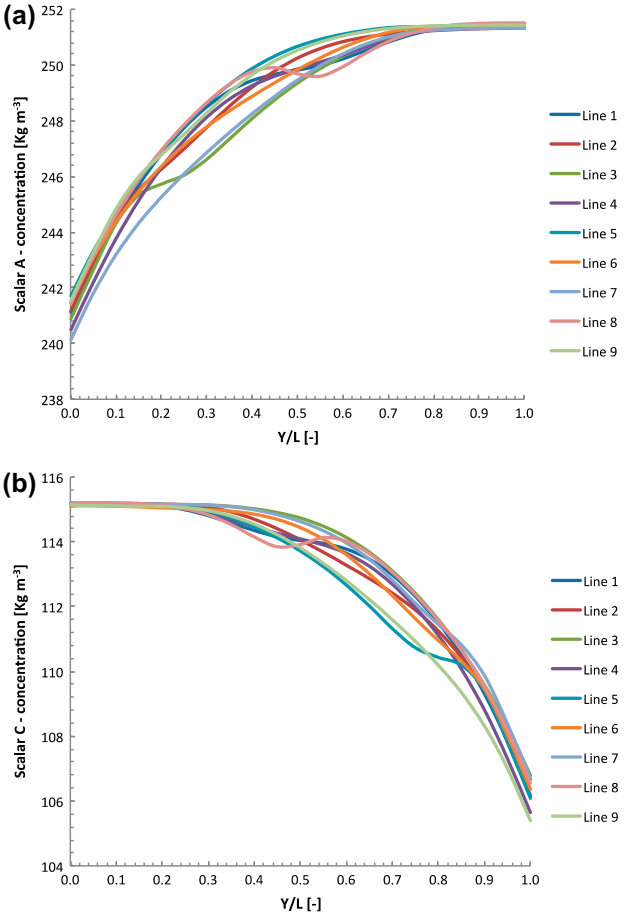

Fig. 18. Concentration profile of (a) scalar A and (b) scalar C along the nine lines for the case of a residence time = 60 s. Overlapped spacer-filled channel.

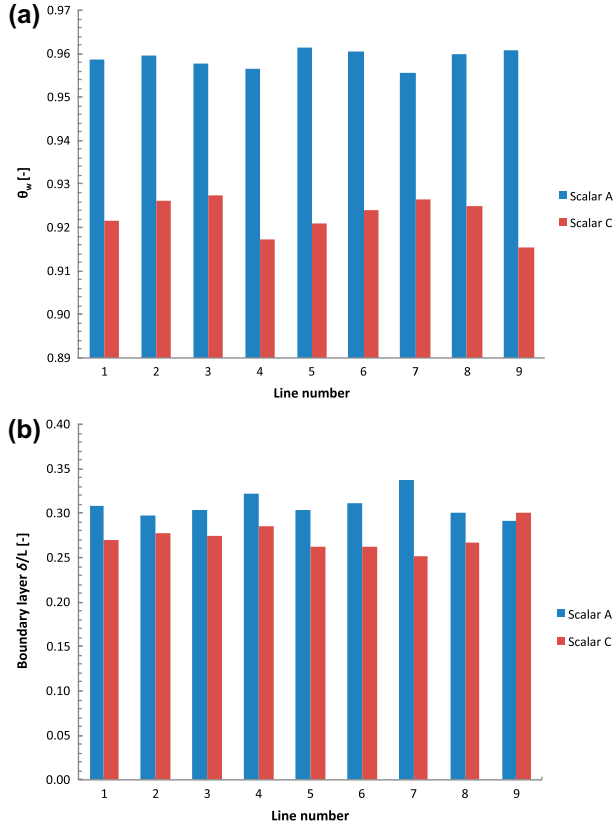

Fig. 19. θ_w (a) and δ (b) vs. residence time along the monitoring line 1. Overlapped spacer-filled channel.

to the role of the convective fluxes that increase as the flow rate increases. As a matter of fact, as the flow

rate increases, the fluid velocity near the filaments increases more than the velocity in the central part of the unit cell [29] thus resulting in different shape of the θ profile.

Also by observing the profiles of θ_w and δ vs. the residence time (not shown for brevity), it appears that the overlapped spacer-filled channel configuration

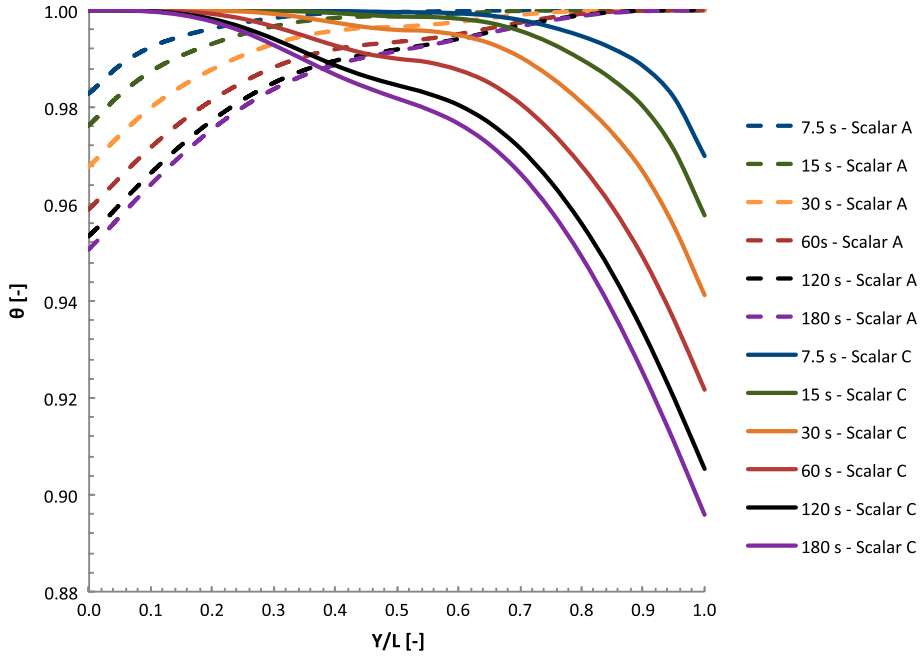

Fig. 20. θ trends along the monitoring line 1 for different residence times. Overlapped spacer-filled channel.

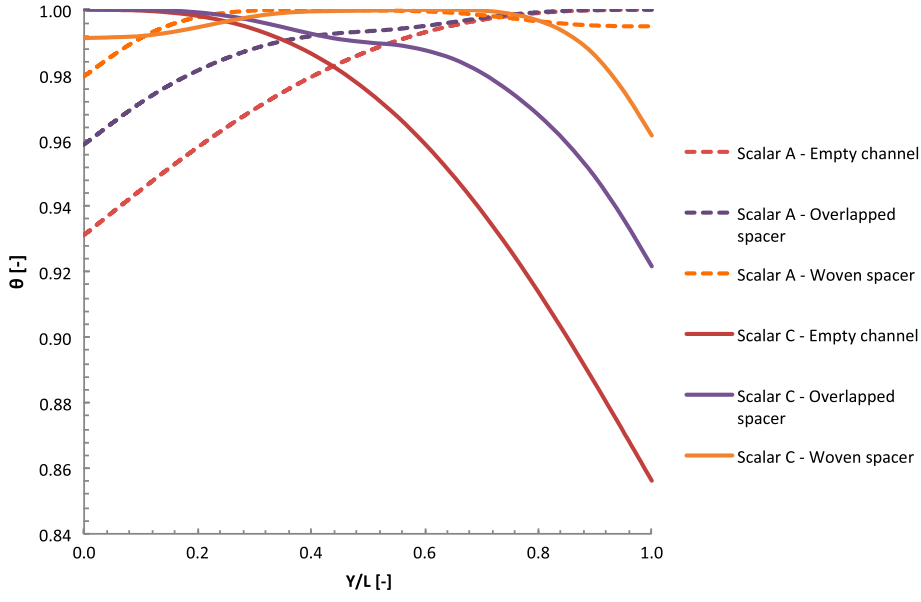

Fig. 21. Comparison (for the three channel configurations) of θ profiles along the line 1 for a flow rate equal to 8×10^{-10} m^3 s^{-1}.

might be an intermediate solution between the woven one and the empty channel.

5.3. Channel geometrical configuration comparison

All the results presented in the previous sections are reported here for comparison purposes aiming at finding the channel geometrical configuration providing the best compromise (among those here investigated) between polarization reduction and pressure drops minimization.

In Fig. 21, a comparison of θ profiles along the line 1 for a flow rate equal to 8×10^{-10} m^3 s^{-1} is reported.

The θ profile for the case of the empty channel has a monotonic first derivative, while an inflection point can be observed for the case of the woven spacer and two changes of concavity for the case of the overlapped spacer. The polarization concentration appears to be more pronounced in the empty channel than in the spacer-filled channels as expected. This can be better observed in Fig. 22 where the θ_w as a function of the residence time

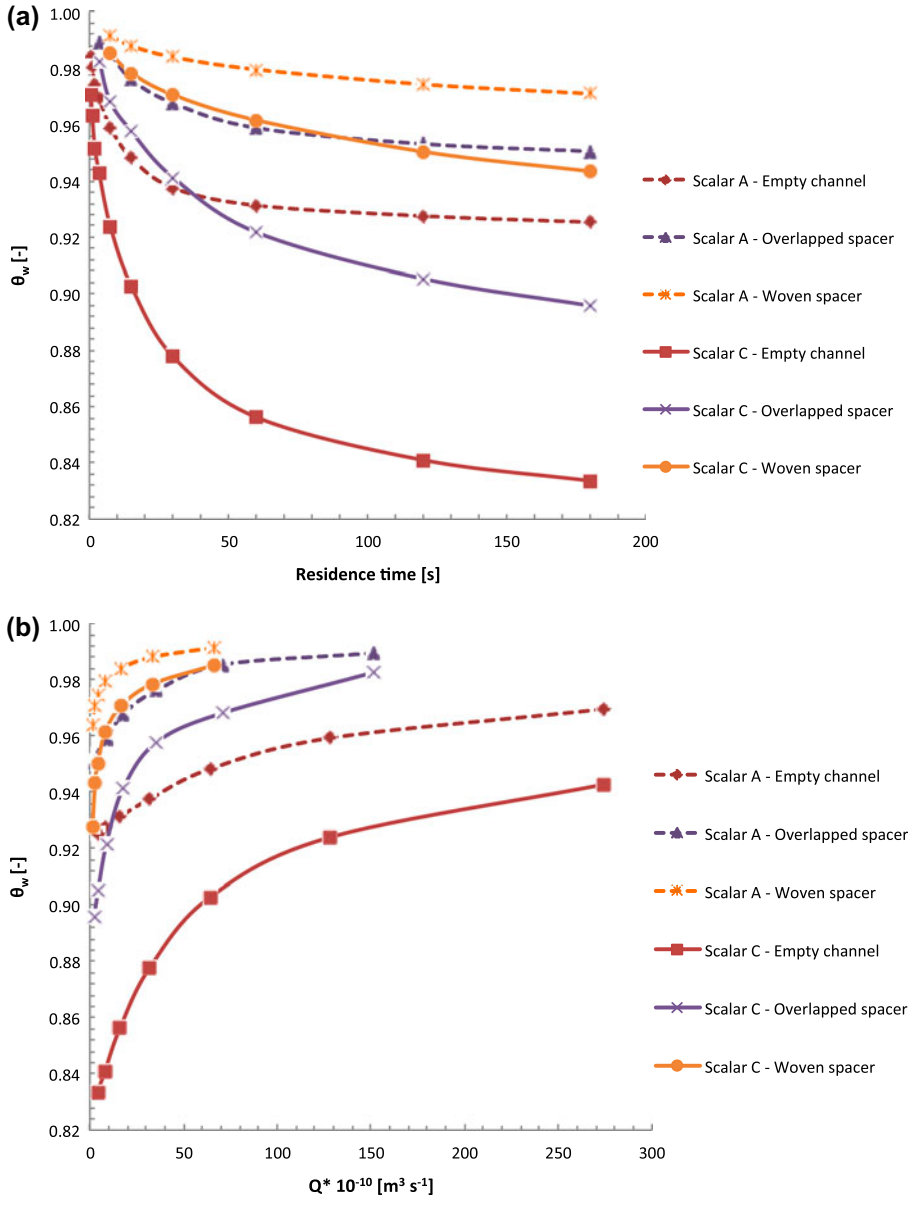

Fig. 22. Comparison (for the three channel configurations) of θ_w along line 1 vs. (a) the residence time of brine water inside the channel and (b) the fluid flow rate.

and the flow rate is shown. At low flow rates the difference between the three configurations is higher: for example, at $Q = 8 \times 10^{-10}$ m^3 s^{-1} the θ_w of the scalar C in the empty channel is 0.84, in the overlapped spacer-filled channel is 0.92, and in the woven spacer-filled channel is 0.94. This difference decreases as the flow rate increases. However, in all the range of residence times investigated, the empty channel is the worst option, while the woven spacer provides the lowest polarization.

Also the thickness of the concentration boundary layer is significantly affected by the channel configuration. In Fig. 23 the trend of δ against the fluid flow rate and residence time for line 1 is reported.

In accordance with the results concerning θ_w, at a given flow rate the empty channel exhibits the largest δ, while the woven spacer-filled channel provides the lowest δ. Here, the differences in δ among the three channel configurations are more marked than the ones observed in θ_w.

The presence of the spacer is known to reduce the concentration polarization phenomena [25], but in turn increases the pressure drops. As an example, on a one hand, the woven spacer provides the lowest polarization factor, on the other hand, it provides also the highest pressure drop and pumping costs. In this regard, it is essential to couple polarization performance with the pressure drops for each channel

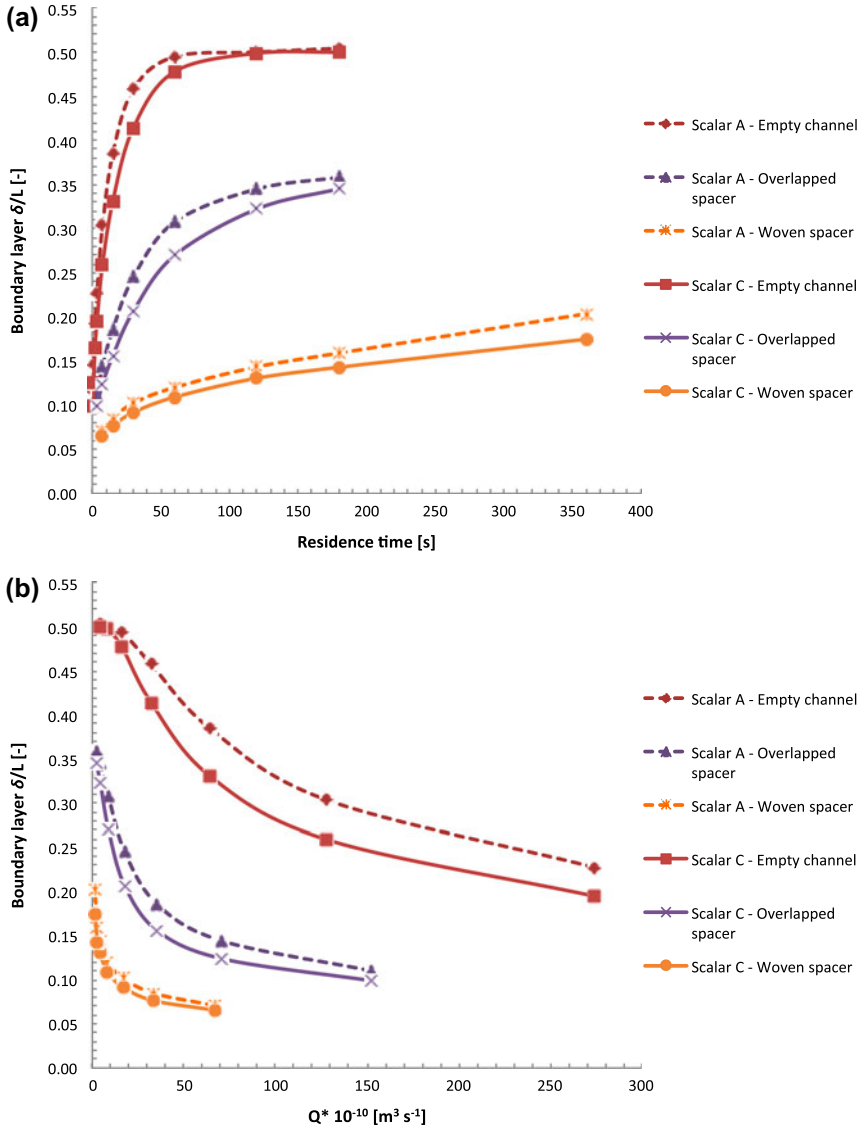

Fig. 23. Comparison (for the three channel configurations) of δ along line 1 as a function of (a) the fluid residence time and (b) the fluid flow rate.

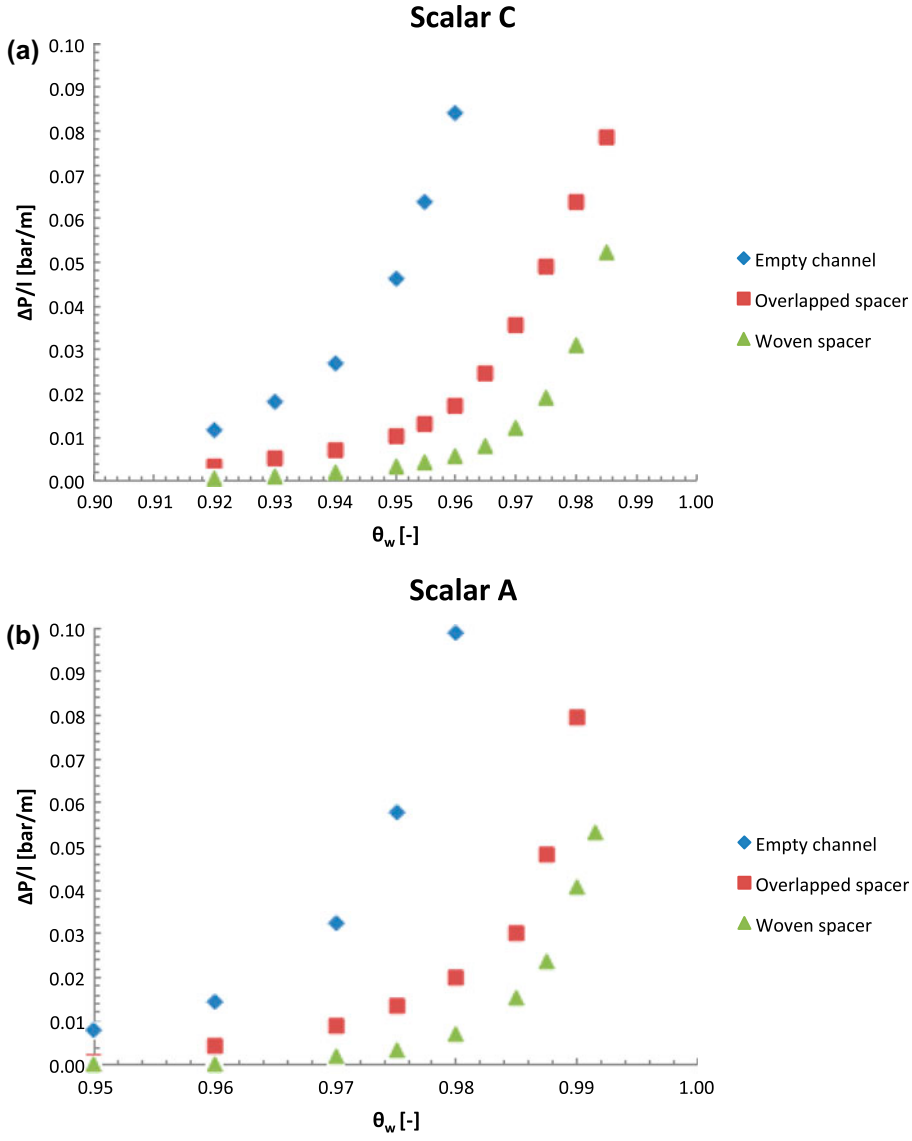

Fig. 24. Pressure drops vs. θ_w for the three channel configurations investigated. Results obtained for (a) scalar C and (b) scalar A.

configuration. Therefore, by coupling the results reported in Fig. 22 with those of Fig. 11, the graphs of Fig. 24 can be obtained.

At a given value of pressure drop, Fig. 24 allows identifying the channel configuration providing the lowest polarization factor. This figure shows that the woven spacer-filled channel is the configuration exhibiting the lowest pressure drops to obtain the same θ_w for the entire range investigated. In other words, such configuration represents the best compromise between the reduction of the concentration polarization and of the pumping costs.

However, it is worth observing that the choice of a specific channel configuration for RED applications should not be performed only on the basis of the above findings since polarization phenomenon may not represent the main responsible of efficiency loss: other aspects (membrane electric resistance, solution electric resistance, electrodic reactions, etc.) should be taken into full account to assess the best geometrical configuration. In this regard, a multi-scale modelling would allow recognizing the phenomenon that mostly controls the efficiency of the RED process. Also, the present preliminary work should be regarded as an investigation

of tracers transport in different channels for RED; therefore, electric aspects (as the local electro-neutrality) have to be also implemented and taken into full account before extrapolating results to real RED applications.

6. Conclusions and suggestions for future work

Net spacers are commonly employed in different membrane separation processes (RO, filtration, MD, RED) to reduce temperature and concentration polarization. The present work investigates the effect of net spacers on concentration polarization in thin channels to be employed as "concentrated" channels in RED applications. In particular, fluid flow and the transport of two passive scalars as feed were simulated by employing the finite volume code Ansys CFX 13. The properties of the two scalars (inlet concentration, diffusivity, flux across the membrane) were chosen in order to mimic the features of positive and negative ions in a concentrated brine for RED operations. Two different computational domains were simulated (i.e. either the unit cell approach or the multi-cell approach). Both transient and steady state simulations were performed.

The multi-cell approach was found to provide results almost identical to those obtained by the unit cell approach in all but the first 1–2 cells of a streamwise strip, thus confirming the viability of the less computationally demanding unit cell approach. The concentration polarization midway between inlet and outlet of the channel was found to decrease as expected when the liquid residence time decreases: for the case of the empty channel this is due to the reduction of the bulk concentration since no velocity components orthogonal to the membrane are present. The presence of a spacer inside the channel allows such velocities to arise thus enhancing the polarization reduction. The spacer also yields a more complex velocity field leading to a less homogenous distribution of the scalar concentration at the membrane surface.

Among the two spacers studied (overlapped and woven), the woven spacer was found to provide a lower polarization at the cost of a higher pressure drop. However, by coupling the polarization and pressure drop data for the three configurations investigated, the woven spacer-filled channel was found to require the lowest pressure drops to obtain the same *wall concentration polarization coefficient* θ_w in the entire range of flow rates investigated here.

This work should be regarded as an investigation of scalar transport in different channels for RED rather than an attempt to simulate the transport of real ions. Future work will address the modelling of real ions within the channel along with the inclusion of their migrative transport.

Acknowledgements

This work has been performed within the REAPower (Reverse Electrodialysis Alternative Power production) project, funded by the EU-FP7 programme (Project Number: 256736)—website www.reapower.eu.

Notation

C	—	scalar concentration (kg m^{-3})
C_{max}	—	maximum scalar concentration along a given monitoring line (kg m^{-3})
C_w	—	concentration on the membrane surface (kg m^{-3})
D_i	—	diffusion coefficient of the salt i (m^2 s^{-1})
$D^\circ_{Cl^-}$, $D^\circ_{Na^+}$	—	infinite dilution diffusion coefficients (m^2 s^{-1})
D_A, D_C	—	diffusion coefficient of scalar A and C at the brine concentration (m^2 s^{-1})
F	—	force for unit volume (N m^{-3})
P	—	pressure (Pa)
$\Delta P/l$	—	pressure drops for unit length (bar m^{-1})
Q	—	flow rate (m^3 s^{-1})
Re	—	Reynolds number (–)
Sc	—	Schmidt number (–)
u	—	velocity (m s^{-1})

Greek letters

δ	—	concentration boundary layer thickness (m)
μ	—	viscosity (Pa s)
ρ	—	density (kg m^{-3})
θ	—	local concentration polarization coefficient (–)
θ_w	—	wall concentration polarization coefficient (–)
τ	—	residence time (s)

References

[1] A. Cipollina, M.G. Di Sparti, A. Tamburini, G. Micale, Development of a membrane distillation module for solar energy seawater desalination, Chem. Eng. Res. Des. 90 (2012) 2101–2121.
[2] R.E. Pattle, Production of electric power by mixing fresh and salt water in the hydroelectric pile, Nature 174 (1954) 660.
[3] J.W. Post, H.V.M. Hamelers, C.J.N. Buisman, Energy recovery from controlled mixing salt and fresh water with a reverse electrodialysis system, Environ. Sci. Technol. 42 (2008) 5785–5790.
[4] S. Loeb, Production of energy from concentrated brines by pressure retarded osmosis. 1. Preliminary technical and economic correlations, J. Membr. Sci. 1 (1976) 49–63.

[5] J.W. Post, J. Veerman, H.V.M. Hamelers, G.J.W. Euverink, S.J. Metz, K. Nymeijer, C.J.N. Buisman, Salinity-gradient power: Evaluation of pressure-retarded osmosis and reverse electrodialysis, J. Membr. Sci. 288 (2007) 218–230.
[6] A. Achilli, A.E. Childress, Pressure retarded osmosis: From the vision of Sidney Loeb to the first prototype installation—Review, Desalination 261 (2010) 205–211.
[7] W. Finley, E. Pscheidt, Hydrocratic Generator, US Patent 6, 313, 545 B1, (2001).
[8] M. Olsson, G.L. Wick, J.D. Isaacs, Salinity gradient power: Utilizing vapor pressure differences, Science 206 (1979) 452–454.
[9] D. Brogioli, R. Zhao, P.M. Biesheuvel, A prototype cell for extracting energy from a water salinity difference by means of double layer expansion in nanoporous carbon electrodes, Energ. Environ. Sci. 4 (2011) 772–777.
[10] R.A. Rica, R. Ziano, D. Salerno, F. Mantegazza, M.Z. Bazant, D. Brogioli, Electro-diffusion of ions in porous electrodes for capacitive extraction of renewable energy from salinity differences, Electrochim. Acta 92 (2013) 304–314.
[11] F. La Mantia, M. Pasta, H.D. Deshazer, B.E. Logan, Y. Cui, Batteries for efficient energy extraction from a water salinity difference, Nano Lett. 11 (2013) 1810–1813.
[12] R.E. Lacey, Energy by reverse electrodialysis, Ocean Eng. 7 (1980) 1–47.
[13] E. Brauns, W. De Wilde, B. Van den Bosch, P. Lens, L. Pinoy, M. Empsten, On the experimental verification of an electrodialysis simulation model for optimal stack configuration design through solver software, Desalination 249 (2009) 1030–1038.
[14] M. Tedesco, A. Cipollina, A. Tamburini, G. Micale, J. Helsen, M Papapetrou, Reapower: Use of desalination brine for power production through reverse electrodialysis, Desalin. Water Treat. (2014, in press), doi: 10.1080/19443994.2014.934102.
[15] M. Tedesco, A. Cipollina, A. Tamburini, I.D.L. Bogle, G. Micale, A simulation tool for analysis and design of reverse electrodialysis using concentrated brines, Chem. Eng. Res. Des. (2014, in press), doi:10.1016/j.cherd.2014.05.009.
[16] J. Kim, S.J. Kim, D.-K. Kim, Energy harvesting from salinity gradient by reverse electrodialysis with anodic alumina nanopores, Energy 51 (2013) 413–421.
[17] O. Scialdone, A. Albanese, A. D'Angelo, A. Galia, C. Guarisco, Investigation of electrode material—Redox couple systems for reverse electrodialysis processes. Part II: Experiments in a stack with 10–50 cell pairs, J. Electroanal. Chem. 704 (2013) 1–9.
[18] B.E. Logan, M. Elimelech, Membrane-based processes for sustainable power generation using water, Nature 488 (2012) 313–319.
[19] E. Brauns, Towards a worldwide sustainable and simultaneous large-scale production of renewable energy and potable water through salinity gradient power by combining reversed electrodialysis and solar power? Desalination 219 (2008) 312–323.
[20] REAPower (Reverse Electrodialysis Alternative Power production) project, funded by the EU-FP7 programme (Project Number: 256736). Available from: www.reapower.eu.
[21] A. Cipollina, G. Micale, L. Rizzuti, Membrane distillation heat transfer enhancement by CFD analysis of internal module geometry, Desalin. Water Treat. 25 (2011) 195–209.
[22] M. Shakaib, S.M.F. Hasani, I. Ahmed, R.M. Yunus, A CFD study on the effect of spacer orientation on temperature polarization in membrane distillation modules, Desalination 284 (2012) 332–340.
[23] S. Al-Sharif, M. Albeirutty, A. Cipollina, G. Micale, Modelling flow and heat transfer in spacer-filled membrane distillation channels using open source CFD code, Desalination 311 (2013) 103–112.
[24] D.E. Wiley, D.F. Fletcher, Techniques for computational fluid dynamics modelling of flow in membrane channels, J. Membr. Sci. 211 (2003) 127–137.
[25] S. Wardeh, H.P. Morvan, CFD simulations of flow and concentration polarization in spacer-filled channels for application to water desalination, Chem. Eng. Res. Des. 86 (2008) 1107–1116.
[26] J.L.C. Santos, V. Geraldes, S. Velizarov, J.G. Crespo, Investigation of flow patterns and mass transfer in membrane module channels filled with flow-aligned spacers using computational fluid dynamics (CFD), J. Membr. Sci. 305 (2007) 103–117.
[27] M. Shakaib, S.M.F. Hasani, M. Mahmood, CFD modeling for flow and mass transfer in spacer-obstructed membrane feed channels, J. Membr. Sci. 326 (2009) 270–284.
[28] M.H. Dirkse, W.K.P. van Loon, J.D. Stigter, J.W. Post, J. Veerman, G.P.A. Bot, Extending potential flow modelling of flat-sheet geometries as applied in membrane-based systems, J. Membr. Sci. 325 (2008) 537–545.
[29] A. Tamburini, G. La Barbera, A. Cipollina, M. Ciofalo, G. Micale, CFD simulation of channels for direct and reverse electrodialysis, Desalin. Water Treat. 48 (2012) 370–389.
[30] L. Gurreri, A. Tamburini, A. Cipollina, G. Micale, CFD analysis of the fluid flow behavior in a reverse electrodialysis stack, Desalin. Water Treat. 48 (2012) 390–403.
[31] L. Gurreri, A. Tamburini, A. Cipollina, G. Micale, M. Ciofalo, CFD simulation of mass transfer phenomena in spacer filled channels for reverse electrodialysis applications, Chem. Eng. Trans. 32 (2013) 1879–1884.
[32] L. Gurreri, A. Tamburini, A. Cipollina, G. Micale, M. Ciofalo, CFD prediction of concentration polarization phenomena in spacer-filled channels for reverse electrodialysis, J. Membr. Sci. 468 (2014) 133–148.
[33] E. Brauns, Finite elements-based 2D theoretical analysis of the effect of IEX membrane thickness and salt solution residence time on the ion transport within a salinity gradient power reverse electrodialysis half cell pair, Desalin. Water Treat. 51 (2013) 6429–6443.
[34] S.K. Karode, A. Kumar, Flow visualization through spacer filled channels by computational fluid dynamics-I: Pressure drop and shear rate calculations for flat sheet geometry, J. Membr. Sci. 193 (2001) 69–84.
[35] A. Tamburini, P. Pitò, A. Cipollina, G. Micale, M. Ciofalo, A thermochromic liquid crystals image analysis technique to investigate temperature polarization in spacer-filled channels for membrane distillation, J. Membr. Sci. 447 (2013) 260–273.
[36] A. Tamburini, G. Micale, M. Ciofalo, A. Cipollina, Experimental analysis via thermochromic liquid

crystals of the temperature local distribution in membrane distillation modules, Chem. Eng. Trans. 32 (2013) 2041–2046.
[37] G. Schock, A. Miquel, Mass transfer and pressure loss in spiral wound modules, Desalination 64 (1987) 339–352.
[38] ANSYS Europe Ltd., ANSYS CFX User's Guide, 2011.
[39] A. Tamburini, A. Cipollina, G. Micale, A. Brucato, M. Ciofalo, CFD simulations of dense solid-liquid suspensions in baffled stirred tanks: Prediction of suspension curves, Chem. Eng. J. 178 (2011) 324–341.
[40] A. Tamburini, A. Cipollina, G. Micale, A. Brucato, M. Ciofalo, CFD simulations of dense solid–liquid suspensions in baffled stirred tanks: Prediction of the minimum impeller speed for complete suspension, Chem. Eng. J. 193–194 (2012) 234–255.
[41] S.V. Patankar, Numerical Heat Transfer and Fluid Flow, Hemisphere Publishing Corp., Washington, DC, 1980.
[42] C.M. Rhie, W.L. Chow, Numerical study of the turbulent flow past an airfoil with trailing edge separation, AIAA J. 21 (1983) 1525–1532.
[43] B.R. Hutchinson, G.D. Raithby, A multigrid method based on the additive correction strategy, Numer. Heat Transfer 9 (1986) 511–537.
[44] J. Veerman, M. Saakes, S. Metz, G. Harmsen, Reverse electrodialysis: A validated process model for design and optimization, Chem. Eng. J. 166 (2010) 256–268.
[45] M. Tedesco, A. Cipollina, A. Tamburini, W. van Baak, G. Micale, Modelling the reverse electrodialysis process with seawater and concentrated brines, Desalin. Water Treat. 49 (2012) 404–424.
[46] L. Gurreri, M. Ciofalo, A. Cipollina, A. Tamburini, W. Van Baak, G. Micale, CFD modelling of profiled-membrane channels for reverse electrodialysis, Desalin. Water. Treat. (2014, in press), doi: 10.1080/19443994.2014.940651.
[47] R.A. Robinson, R.H. Stockes, Electrolyte Solutions, second ed., Butterworths Scientific Publication, London, 1959.
[48] Z.X. Yuan, W.Q. Tao, Q.W. Wang, Numerical prediction for laminar forced convection heat transfer in parallel-plate channels with streamwise-periodic rod disturbances, Int. J. Numerical Meth. Fluids 28 (1998) 1371–1387.
[49] Y.L. Li, K.L. Tung, CFD simulation of fluid flow through spacer-filled membrane module: Selecting suitable cell types for periodic boundary conditions, Desalination 233 (2008) 351–358.
[50] M. Ciofalo, I. Di Piazza, J.A. Stasiek, Investigation of flow and heat transfer in corrugated-undulated plate heat exchangers, Heat Mass Transfer 36 (2000) 449–462.
[51] D. Molyneux, N. Bose, Escort tug at large yaw angle: Comparison of CFD predictions with experimental data: Transactions of the Royal Institution of Naval Architects Part B, Int. J. Small Craft Technol. 150 (2008) 41–60.
[52] H.I. Oguntade, G.E. Andrews, A. Burns, D. Ingham, M. Pourkashanian, CFD predictions of single row film cooling with inclined holes: Influence of hole outlet geometry, in: Proceedings of the ASME Turbo Expo 4 (2010) 1371–1385.
[53] A. Tamburini, A. Cipollina, G. Micale, A. Brucato, M. Ciofalo, CFD simulations of dense solid-liquid suspensions in baffled stirred tanks: Prediction of solid particle distribution, Chem. Eng. J. 223 (2013) 875–890.
[54] R.B. Bird, W.E. Stewart, E.N. Lightfoot, Transport Phenomena, second ed., Wiley, New York, NY, 2002.
[55] D.A. Vermaas, M. Saakes, K. Nijmeijer, Doubled power density from salinity gradients at reduced intermembrane distance. Environ. Sci. Technol. 45 (2011) 7089–7095.